Food Chemistry: X 25 (2025) 102094

Contents lists available at ScienceDirect

Food Chemistry: X

journal homepage: www.sciencedirect.com/journal/food-chemistry-x

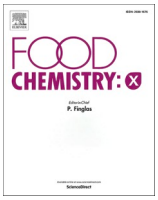

Efficient voltammetric platform combining a molecularly imprinted polymer and silver-nanoparticle-decorated black phosphorus nanosheets for selective determination of Gatifloxacin

Jingtao Wu [a], Yonghui Xia [b], Tianyu Wang [a], Yafeng Zhang [a], Guangli Li [a,*]

[a] Hunan Key Laboratory of Biomedical Nanomaterials and Devices, College of Life Science and Chemistry, Hunan University of Technology, Zhuzhou 412007, China
[b] Zhuzhou Institute for Food and Drug Control, Zhuzhou 412000, China

ARTICLE INFO

Keywords:
Molecularly imprinted polymer
Poly(pyrrole)
Ag nanoparticles
Black phosphorus nanosheets
Gatifloxacin determination

ABSTRACT

An ultrasensitive and selective voltammetric platform combined a molecularly imprinted poly(pyrrole) membrane with Ag-nanoparticle-functionalized black phosphorus nanosheets (MIP/BPNS-AgNPs) was developed for trace GAT detection. The physicochemical properties of the MIP/BPNS-AgNPs were studied by various spectroscopic and electrochemical techniques. BPNS-AgNPs improved the ambient stability and electrochemical activity of the BPNS and possessed a large surface area for accommodating abundant templates to produce specific imprinted sites. The resulting MIP/BPNS-AgNP-modified glassy carbon electrode (GCE) greatly enhanced voltammetric responses for GAT. The MIP/BPNS-AgNP/GCE exhibited admirable GAT determination performance, with two linear responses (0.001–1 and 1–50 μM), high sensitivity (9.965 and 0.5378 μA μM^{-1}), and a low detection limit of 0.2 nM. In addition, the MIP electrode could selectively detect GAT in complex matrices and retain roust responses for a month. The applicability of MIP/BPNS-AgNP/GCE toward the detection of GAT in pharmaceutical formulations, milk, and human serum was verified with satisfactory results.

1. Introduction

Gatifloxacin (GAT), a fourth-generation quinolone antibiotic, exhibits broad-spectrum antibacterial activity against a variety of Gram-negative and Gram-positive bacteria by inhibiting DNA gyrase (Wan, Wu, Zhang, & Zhang, 2022). GAT is commonly used to treat urinary tract, respiratory tract, osteomyelitis, gastrointestinal, skin, and soft-tissue infections in humans and food-producing animals (Yu, Yue, Xu, & Jiang, 2020). However, due to its improper use and incomplete metabolism, GAT residues are accumulating in animal-derived foods and ecological environments, posing a huge threat to human health (Van Doorslaer, Dewulf, Van Langenhove and Demeestere, 2014). Excessive GAT intake may enhance pathogen resistance to antibiotics (Uddin et al., 2021). Thus, the development of efficient methods for sensing trace levels of GAT in medicines, foods and physiological fluids is of crucial importance.

Current methods for GAT detection include UV–visible spectrophotometry (Sversut et al., 2017), high-performance liquid chromatography (HPLC) (Saad, Essam, Elzanfaly, & Amer, 2020), fluorometry (Sumalatha & Ayodhya, 2023), and capillary electrophoresis (Ma et al., 2021). These methods have been widely used and accepted. However, they still entail disadvantages of cumbersome procedures, time consumption, and high cost. Electrochemical methods have attracted increasing attention in sensing applications owing to their advantages of low cost, quick response, convenient operation, high sensitivity, and ease of miniaturization (Li et al., 2022a,b; T. Wang et al., 2024; Y. Wang et al., 2022). Electrochemical methods have proven to be effective toward the detection of GAT (Jiang et al., 2019; Li et al., 2024a; Li et al., 2024b; Taherizadeh, Jahani, Moradalizadeh, & Foroughi, 2023; Wan et al., 2023). Despite the progress, robust and selective detection of GAT in complicated matrices remains a significant challenge.

Molecularly imprinted polymers (MIPs) are typically introduced into electrochemical sensors for selectivity improvement. MIPs achieve selectivity by specifically binding target molecules at templated recognition sites (Cui, Liu, Liu, Liu, & Zhang, 2020; Wu et al., 2021). MIPs outperform biological recognition components in terms of cost, tunability, reusability, environmental tolerance, and shelf life. Although MIPs have been used in electrochemical sensors (Hasseb, Abdel Ghani, Shehab, & El Nashar, 2022; Wu et al., 2021), most examples have limitations such as low electrical conductivity, weak binding ability, and

* Corresponding author.
E-mail address: guangli010@hut.edu.cn (G. Li).

https://doi.org/10.1016/j.fochx.2024.102094
Received 17 October 2024; Received in revised form 5 December 2024; Accepted 11 December 2024

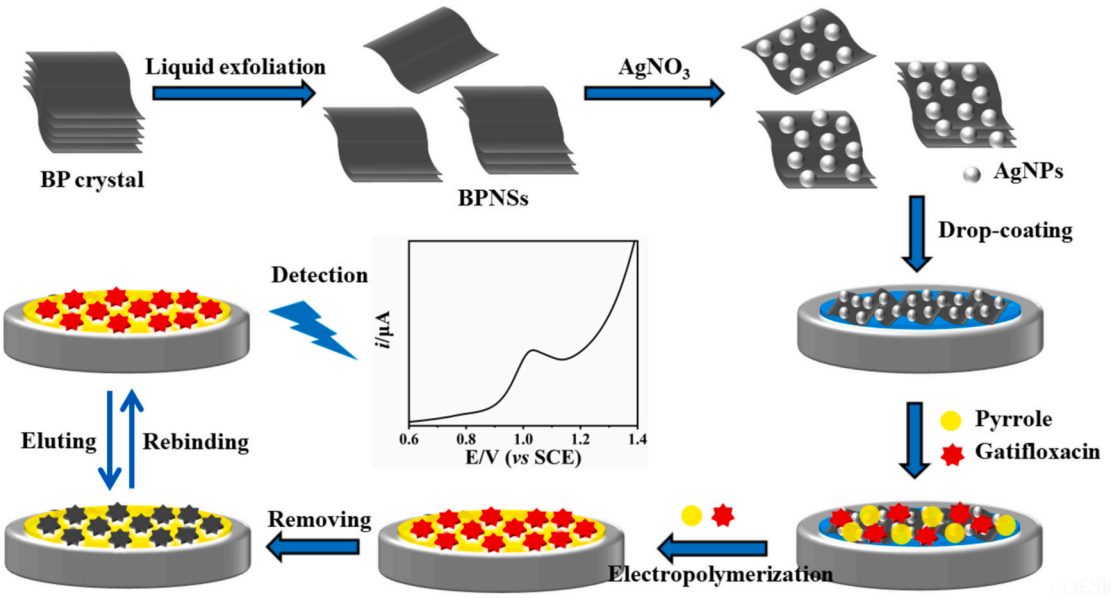

Scheme 1. Schematic diagram of the fabrication process of MIP/BPNS-AgNP/GCE.

incomplete template removal (Razavipanah, Alipour, Deiminiat, & Rounaghi, 2018; Xu et al., 2018). Nanostructured materials with large specific surface areas have been employed as electrode substrates to overcome these shortcomings.

Black phosphorus (BP) is a two-dimensional layered nanomaterial that shows great promise for deployment in MIP-based voltammetric platforms because of its large specific surface area, anisotropic electrical properties, and excellent electroactivity (Anju, Ashtami, & Mohanan, 2019; Ge, Xia, & Guo, 2019; Li et al., 2021). BP has been employed as a support material to construct efficient MIP-based electrochemical sensors for ascorbic acid (AA) (Zhang, Li, Xu, & Wen, 2018) and norfloxacin (NOR) (Li et al., 2022a; Li et al., 2022b). However, the instability of BP in ambient environment significantly hinders its application (Caporali et al., 2020; Chen et al., 2022; Tian et al., 2020). The functionalization of BP with conducting polymers, noble metals, metal oxides and metal–organic frameworks has been reported (Abate et al., 2018; Li et al., 2021; Liu et al., 2021; Qiu et al., 2022). Nanoparticulate noble metals such as Au, Ag, and Pt have unique advantages among these modifiers, including excellent catalytic activity, facile synthesis, and extraordinary stability (Shoueir, Mohanty, & Janowska, 2022; Takeuchi et al., 2021; Wang et al., 2022). The strong interaction between the non-bonded electrons of BP and metal ions promotes the attachment of metal nanoparticles and improves stability (Liu, Zhu, Ban, Wang, & Zhu, 2021). For example, Liu, Luo, Jiang, Li, and Yang (2020) prepared a biosensor using gold nanoparticles (AuNPs) to stabilize BP nanosheets (BPNS) and applied it to the capture and determination of circulating tumor cells in whole blood with a limit of detection (LOD) of 2 cell mL^{-1}. Wang et al. (2022) prepared AgNP-modified BPNS as sensing elements to recognize trace NO_2 at room temperature. BP-Ag nanocomposites are superior to pure BPNS in terms of sensitivity, speed of response, recovery level, and stability in the detection of trace NO_2. Cho, Koh, Yoo, and Jung (2017) proposed the use of Au and Pt nanoparticles to improve the stability of BP for NO_2 sensing. However, an MIP sensor based on Ag-functionalized BPNS for the detection of antibiotics has not been reported.

Herein, we report a novel MIP voltammetric platform for the efficient detection of GAT based on a molecularly imprinted poly(pyrrole) (PPy) membrane attached to a AgNP-modified BPNS substrate (MIP/BPNS-AgNP). The BPNS-AgNP substrates were synthesized by an environment-friendly one-step reduction procedure and drop-cast onto the surface of a glassy carbon electrode (GCE). PPy was then coated onto the surface of BPNS-AgNP/GCE from an aqueous solution also containing the target GAT analyte to create the MIP/BPNS-AgNP/GCE. Removal of the templates leaves behind molecularly imprinted sites capable of binding and sensing GAT. This paper describes the fabrication and characterization of the MIP/BPNS-AgNP/GCEs and their applications to the ultrasensitive determination of GAT in pharmaceuticals, milk, and human serum.

2. Materials and methods

2.1. Materials and reagents

Bulk BP crystals were supplied by Shenzhen 6Carbon Technology Co., Ltd., China. Marbofloxacin (MAR) and GAT were purchased from Shanghai Macklin Biochemical Co. Ltd., China. Lomefloxacin hydrochloride (LOME), ofloxacin (OFL), NOR, levofloxacin (LEV), enrofloxacin (ENR), penicillin G sodium (PEN-G), amoxicillin (AMO), tetracycline hydrochloride (TET), pyrrole (Py), *N*-methylpyrrolidone (NMP), dopamine hydrochloride (DOP), AA, lysine (LYS), and uric acid (UA) were purchased from Aladdin Reagent Co. Ltd. (Shanghai, China). Anhydrous glucose was purchased from Kemio Chemical Reagent Co. Ltd. (Tianjin, China). Anhydrous ethanol, $AgNO_3$, $K_3Fe(CN)_6$, $K_4Fe(CN)_6$, KCl, NaH_2PO_4, and Na_2HPO_4 were supplied by Sinopharm Chemical Reagent Co. Ltd. (Shanghai, China). Deionized water with a resistivity of 18.2 MΩ cm was used for the preparation of all solutions.

2.2. Synthesis of BPNS-AgNP

Few-layer BPNS were fabricated from bulk BP crystals using an ultrasound-assisted liquid-phase stripping method. The detail procedure (Supplementary Materials S1) was referred to our previous study (Li et al., 2022b). BPNS-AgNP was prepared in situ. 1 mL $AgNO_3$ solution (5 mM) was added to 1 mL BPNS dispersion (0.4 mg mL^{-1}) in an Ar atmosphere and stirred ceaselessly for 30 min. The suspension was centrifuged at 12,000 rpm for 8 min, and the as-collected solids were cleaned four times with absolute ethanol. The final product was redispersed in absolute ethanol and stored at 4 °C.

2.3. Fabrication of MIP/BPNS-AgNP/GCE

The surface of bare GCE was thoroughly polished with a 0.05 μm α-Al_2O_3 slurry to give a mirror-like appearance. The GCE was

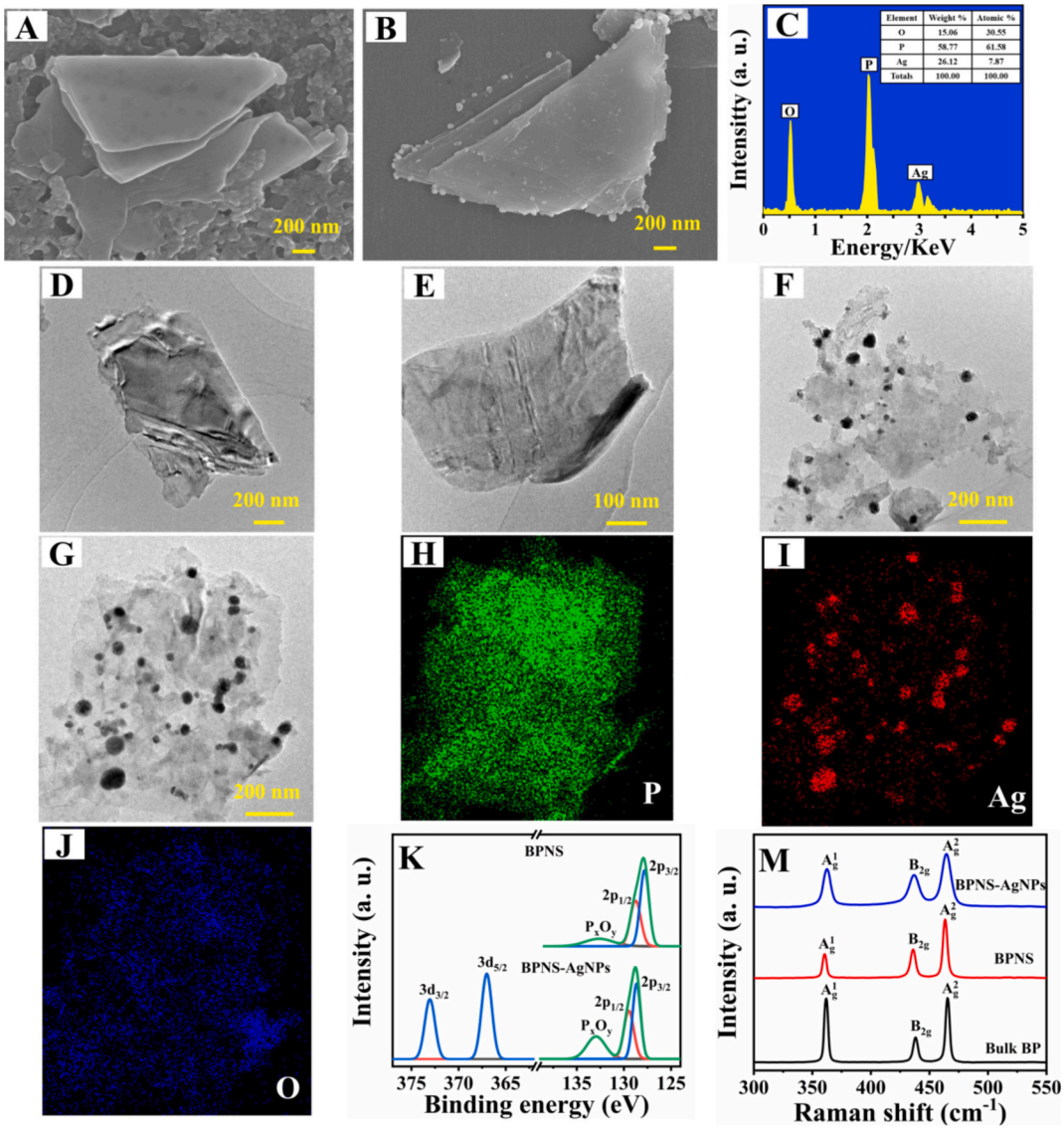

Fig. 1. SEM images of (A) BPNS and (B) BPNS-AgNP; (C) EDX profile of BPNS-AgNP; TEM images of (D, E) BPNS and (F, G) BPNS-AgNP; (H-J) HAADF-STEM images of BPNS-AgNP; (K) XPS profiles of BPNS and BPNS-AgNP; (M) Raman spectra of BP, BPNS, and BPNS-AgNP.

sequentially rinsed with deionized water, anhydrous ethanol, and deionized water, followed by ultrasonication and drying under infrared light.

MIP/BPNS-AgNP/GCE was prepared by an in-situ electropolymerization method using GAT as template (Scheme 1) (Liu, Su, Wu, & Shen, 2021). Typically, 4 μL BPNS-AgNP suspension was casted onto the GCE surface and adequately dried in the inert gas atmosphere. The resultant BPNS-AgNP/GCE platform was immersed in a mixture of 0.01 M GAT and 0.02 M Py, and continuous cyclic voltammetry (CV) scans were performed from −0.2 to 1.6 V at a scanning rate of 0.1 V s^{-1} to form a GAT-imprinted PPy membrane. The templates embedded into the PPy matrices were extracted by electrochemical over-oxidation followed by mixed-solvent elution. Specifically, the MIP/BPNS-AgNP/GCE was immersed in a blank PBS (0.1 M), and five continuous CV scans were conducted at 1.0–1.5 V to overoxidize PPy. Then the over-oxidized MIP/BPNS-AgNP/GCE was immersed in an ethanol:1 M NaOH (2:1, *v*/v) for 10 min to completely extract the templates. As a result, plentiful imprinted sites were grown onto the over-oxidized PPy membrane to allow the selective recognition and quantitation of GAT. The residual templates were recovered for reuse through 10 min elution with ethanol:1 M NaOH (2:1, v/v). Non-imprinted (NIP) electrodes were also prepared for comparative analysis. NIP electrodes were prepared by the same approach in the absence of GAT.

2.4. Material characterization

The morphologies of BPNS, MIP/BPNS-AgNP and NIP/BPNS-AgNP were observed through field-emission scanning electron microscope (ZEISS Sigma 300, Jena, Germany) coupled with energy-dispersive X-ray spectrometer (X-MaxN, Oxford Instruments, UK). Transmission electron microscopy (TEM) of BPNS and BPNS-AgNP was performed to analyze their microstructures using a JEM-2100F microscope (JEOL, Tokyo, Japan). Before SEM and TEM analysis, the specimens were sputtered with very thin gold layers. Raman spectra of BP, BPNS, and BPNS-AgNP were scanned in the range of 200–800 cm^{-1} using a R532 model Raman spectrometer (EnSpectr, USA) fitted with a 632.8 nm He-Ne laser (25 mW). Chemical compositions and valence states of the BPNS and BPNS-AgNP were analyzed on a KAlpha X-ray photoelectron system (Thermo Fisher Scientific, UK) using a monochromatic Al-Kα X-ray source (1486.71 eV).

2.5. Electrochemical studies

All electrochemical measurements were performed on a CHI 660e electrochemical workstation (Chenhua Instrument company, Shanghai, China) with a classic three-electrode system, which comprising a MIP/BPNS-AgNP/GCE working electrode, a platinum wire auxiliary electrode, and a saturated calomel reference electrode. Unless otherwise stated, 0.1 M phosphate buffered saline (PBS, pH 5.5) was used as the supporting electrolyte. In order to study their electrochemical behavior, CV curves and electrochemical impedance spectroscopy (EIS) plots of different electrodes were recorded in a solution of 0.5 mM $[Fe(CN)_6]^{3-/4-}$ and 0.1 M KCl. Linear sweep voltammetry (LSV) was conducted to quantitate GAT. MIP/BPNS-AgNP/GCE was incubated in 0.1 M PBS containing various concentrations of GAT for 10 min under agitation. Next, MIP/BPNS-AgNP/GCE was transferred into a blank PBS (0.1 M), and LSV traces were recorded from 0.6 to 1.4 V at a scanning rate of 0.1 V s^{-1} after a 30 s rest period.

2.6. GAT detection in real samples

GAT eye drops (Laopuyuntang Pharmaceutical Co. Ltd., Chuxiong, China) were purchased from local pharmacists. An appropriate amount of GAT eye drops was completely dissolved into 100 mL deionized water to prepare a stock solution (0.01 M). The stock solutions were separately diluted to 0.5 and 5 μM with 0.1 M PBS for the determination of GAT. A standard GAT solution was added to the diluted samples to perform a recovery test. Pure milk (4 % fat) was bought from a shop near our campus (Mengniu®, Inner Mongolia, China) and diluted 50-fold using 0.1 M PBS. Human serum samples were collected from Zhuzhou People's Hospital (Zhuzhou, China) and diluted 100-fold using 0.1 M PBS. A series of GAT standard solutions with different concentrations were spiked into the milk and serum samples for recovery tests.

3. Results and discussion

3.1. Physical characterization of MIP/BPNS-AgNP membrane

The surface morphologies of BPNS and BPNS-AgNP were studied through scanning electron microscopy (SEM). Several layers of BPNSs with uneven sheet structures were observed (Fig. 1A), confirming that bulk BP crystals were delaminated into BPNSs via an ultrasound-assisted liquid-phase exfoliation. Fig. 1B shows that the granular AgNPs were uniformly distributed on the BPNS surface. The elemental composition of BPNS-AgNP was analyzed by energy-dispersive X-ray spectrometry (EDX). Fig. 1C reveals the peaks for P, Ag, and O at 58.77, 26.12, and 15.06 wt%, respectively, indicating the successful synthesis of BPNS-AgNP.

The microscopic structure of BPNS and BPNS-AgNP were further observed through TEM. Typical sheet-like structures of the BPNS are evident in Fig. 1D and E. The TEM images (Fig. 1F and G) show the coverage of granular AgNP on the BPNS. The HAADF-STEM images in Fig. 1H-J confirm the uniform distribution of P, Ag, and O on BPNS-AgNP. The X-ray photoelectron spectroscopy (XPS) spectra of BPNS and BPNS-AgNP were investigated to confirm their chemical compositions and valence states. Fig. 1K shows the P $2p_{3/2}$, P $2p_{1/2}$, and P_xO_y sub-band signals at 129.7, 130.6, and 133.4 eV, respectively, in the spectra of the BPNS and BPNS-AgNP (Liu, Chen, et al., 2021; Liu, Su, et al., 2021). The slight shift and increase in the intensity of the P_xO_y signal in the spectrum of BPNS-AgNP relative to that of the BPNS indicates the oxidation of the BPNS after AgNP formation (Wang et al., 2022). The Ag spectrum can be well deconvoluted into a doublet at 368.4 and 374.4 eV, which is attributed to Ag^0 (Wang et al., 2022). These results indicate the successful synthesis of BPNS-AgNP. The formation of BPNS-AgNP is likely attributed to a redox reaction occurring between BPNS and $AgNO_3$ (Liu, Feng, et al., 2020; Liu, Luo, et al., 2020; Ryder et al., 2016; Wang, Zhang, et al., 2024). Phosphorus atoms on the surface of BPNS can adsorb silver ions, thereby functioning as a reducing agent that converts silver ions (Ag^+) into silver atoms (Ag^0). These reduced silver atoms then aggregate on the surface of BPNS, forming AgNP. The Raman spectra of BP, BPNS, and BPNS-AgNP (Fig. 1M) display three prominent peaks at ca. 365, 435 and 468 cm^{-1}, which is closely associated with one out-of-plane phonon mode (A_g^1) and two in-plane phonon modes (B_{2g} and A_g^2) (Lei et al., 2016). An evident red shift is found in the Raman spectrum of BPNS-AgNP due to the presence of AgNP, demonstrating in-situ grown AgNP onto BPNS.

The morphologies of MIP/BPNS-AgNP/GCE assembly before and after template removal were studied through SEM. Fig. S1A reveals that the MIP/BPNS-AgNP/GCE surface is smooth and flat; this is due to the formation of a compact PPy membrane on the electrode surface. After removing the templates, the MIP/BPNS-AgNP/GCE possessed a distinctly wrinkled structure with small pores (Fig. S1B), indicating the formation of specific cavities in the PPy matrix. These cavities are completely complementary to the template molecule and can selectively recognize and bind GAT. By comparison, the NIP/BPNS-AgNP structure is much rougher than its MIP counterpart before elution (Fig. S1C), and its morphology remains nearly unchanged after elution (Fig. S2D).

3.2. Optimization of detection conditions

3.2.1. Loading volume of BPNS-AgNP

The influence of the quantity of BPNS-AgNP dispersed on the GCE surface was investigated by LSV. Fig. S2A displays that the anodic peak current (i_{pa}) of GAT increases with an increasing quantity of BPNS-AgNP, reaching a maximum at 4 μL, and decreases with the further addition of BPNS-AgNP. This result is attributed to the electron transfer resistance imparted by thick membranes. Thus, the optimum quantity of dispersed BPNS-AgNP is 4.0 μL.

3.2.2. GAT:Py molar ratio

The number of imprinted sites within the PPy membrane is heavily dependent on the GAT:Py molar ratio. Its influence on the GAT peak current is shown in Fig. S2B. As the GAF:Py molar ratio increases from 1:5 to 5:1, i_{pa} increases sharply and then decreases yielding an optimal value of 1:2.

3.2.3. Number of electropolymerization cycles

The number of available imprinting sites and the final sensitivity is closely correlated with the thickness of MIP film, which can be well controlled by the number of electropolymerization cycles. Fig. S2C shows that the GAT peak current increases drastically with the number of electropolymerization cycles increasing from one to five, but roughly plateaus after additional cycles. A possible explanation for this behavior is that the potential templating sites within the membrane become inaccessible beyond a certain polymer thickness. Thus, five electropolymerization cycles were used in all experiments.

3.2.4. Template removal

The complete removal of the template molecules is essential for the development of an efficient sensor, because the rebinding capacity is optimized, and the background signal is reduced. Templates were removed by repeated CV scans and ethanol:1 M NaOH solvent elution. The ethanol:1 M NaOH ratio (*v*/v) and elution time were carefully optimized to achieve efficient template removal. Fig. S2D shows that neither pure ethanol or pure 1 M NaOH completely elutes the templates within the PPy membrane. The highest GAF peak current was achieved at an ethanol:1 M NaOH ratio of 2:1; thus, this ratio was used in all experiments. In a similar manner, the GAT peak current reached the maximum value at an elution time of 15 min (Fig. S2E). The peak current decreases at longer times, because excessive elution destroys the structure of the MIP membrane.

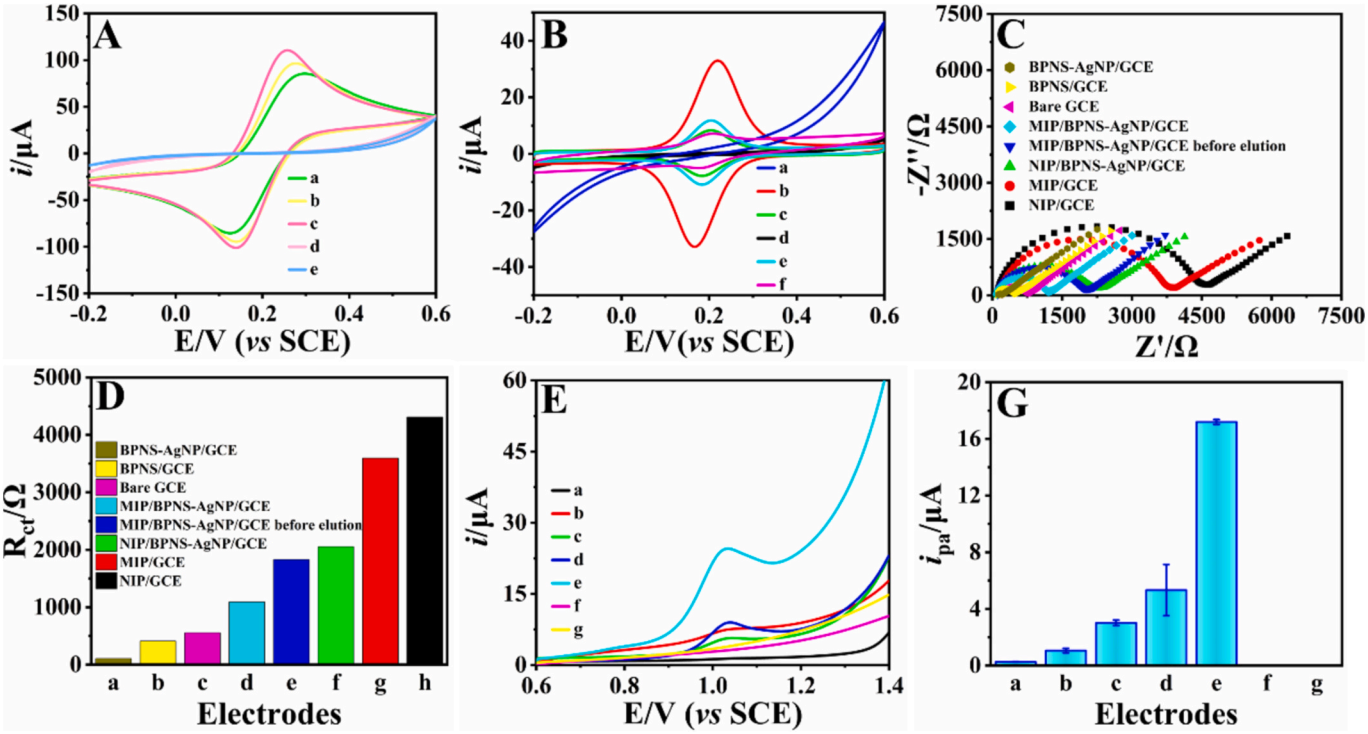

Fig. 2. (A) CV profiles of 5 mM $[Fe(CN)_6]^{3-/4-}$ probe at (a) bare GCE, (b) BPNS/GCE, (c) BPNS-AgNP/GCE, (d) NIP/GCE and (e) NIP/BPNS-AgNP/GCE; (B) CV curves of 5 mM $[Fe(CN)_6]^{3-/4-}$ probe at (a) MIP/BPNS-AgNP/GCE before template removal, (b) MIP/BPNS-AgNP/GCE, (c) MIP/BPNS-AgNP/GCE after incubation with 10 μM GAT, (d) MIP/GCE before template removal, (e) MIP/GCE and (f) MIP/GCE after incubation with 10 μM GAT; (C) Nyquist plots and (D) their corresponding R_{ct} values of 5 mM $[Fe(CN)_6]^{3-/4-}$ probe at the different electrodes; (E) LSV plots of 10 μM GAT recorded using various electrodes and (F) the corresponding GAT peak currents at (a) GCE, (b) BPNS-AgNP/GCE, (c) MIP/GCE, (d) MIP/BPNS/GCE, (e) MIP/BPNS-AgNP/GCE, (f) NIP/GCE, and (g) NIP/BPNS-AgNP/GCE.

3.2.5. Solution pH

The influence of solution pH on the oxidation of 10 μM GAT using MIP/BPNS-AgNP/GCE was studied in 0.1 M PBS. Fig. S2F shows that the oxidation peak shift to more negative potential with increasing buffer pH, which indicates that protons (H^+) are released upon GAT oxidation. The influence of pH on the i_{pa}(GAT) is shown in Fig. S2G. The peak current reaches a maximum at pH 5.5; thus, this pH value was chosen for all experimental studies. This phenomenon can be well explained as follows. GAT has a pK_{a1} of 5.6 for the carboxyl group and a pK_{a2} of 8.8 for the piperazinyl group (Caianelo et al., 2022). At pH 5.5, GAT molecules are in a cationic form, resulting in electrostatic attraction between GAT and MIP/BPNS-AgNP/GCE. At pH lower than 5.5, the presence of an excess of protons in the solution prevents the GAT oxidation, reducing the anodic peak current. At pH higher than 5.5, the anodic peak current of GAT decreases, which may be due to the presence of GAT in the zwitterionic form between pH 5.6 and 8.8 where the anionic form is the only form at pH exceeding 8.8, leading to a more decrease in the anodic peak current of GAT. In addition, the GAT peak potential is negatively proportional to pH (Fig. S2H), and the linear regression equation was $E_{pa}(V) = -0.04618\ pH + 1.281$ ($R^2 = 0.9816$). The slope (46.18 mV pH^{-1}) was close to the theoretical Nernst-equation value (0.0592 V pH^{-1}), demonstrating that equal numbers of electrons and protons are involved in the GAT oxidation.

3.2.6. Incubation time

The binding of GAT to the empty-template MIP membrane relies on the incubation time. Fig. S2I shows that GAT peak current increases with incubation time and reaches a plateau at an optimum value of 10 min, consistent with the refilling of all accessible cavities with GAT.

3.3. Electrochemical properties of MIP/BPNS-AgNP membrane

The preparation process of MIP/BPNS-AgNP/GCE sensor was investigated by CV in a solution comprising 5 mM $[Fe(CN)_6]^{3-/4-}$ and 0.1 M KCl (Fig. 2A). Reversible redox peaks for $[Fe(CN)_6]^{3-/4-}$ probe appeared at the undecorated GCE (curve a) with the anodic and cathodic peak currents (i_{pa} and i_{pc}, respectively) of 90.10 and 92.12 μA, respectively. When the BPNS (curve b) and BPNS-AgNP (curve c) were modified onto the GCE, the i_{pa} and i_{pc} increased. The redox peak currents were the highest for BPNS-AgNP/GCE (i_{pa} = 121.1 μA, i_{pc} = 115.3 μA), indicating that BPNS-AgNP exhibited excellent electrical conductivity and promoted electron transfer. The peak currents for NIP/GCE (curve d) and NIP/BPNS-AgNP/GCE (curve e) were almost undetectable, because the PPy matrix inhibited electron transfer. The performance of MIP/BPNS-AgNP/GCE and MIP/GCE before and after template elution is compared in Fig. 2B. No noticeable redox peaks were seen for either MIP/GCE (curve d) or MIP/BPNS-AgNP/GCE (curve a) before template elution, because the PPy membrane is a poor conductor. Distinct redox peaks were observed for MIP/GCE (curve e) and MIP/BPNS-AgNP/GCE (curve b) after template elution. Here, i_{pa} = 11.18 and i_{pc} = 10.20 μA for MIP/GCE and i_{pa} = 30.96 and i_{pc} = 31.03 μA for MIP/BPNS-AgNP/GCE. After incubation in GAT, i_{pa} and i_{pc} at MIP/GCE (curve f) decreased to 3.823 and 3.186 μA, respectively, and i_{pa} and i_{pc} at MIP/BPNS-AgNP/GCE (curve c) decreased to 7.241 and 6.792 μA, respectively. These results confirm the superior sensing capability of MIP/BPNS-AgNP/GCE. The high conductivity and large surface area of BPNS-AgNP facilitate electron transfer and create conditions for the formation of abundant imprinted cavities.

EIS is an effective technique for studying the kinetics and mass-transport properties of electrode reactions through measurement of the charge transfer resistance (R_{ct}), which is displayed in the form of semicircular Nyquist plots. Fig. 2C shows the Nyquist diagrams of the

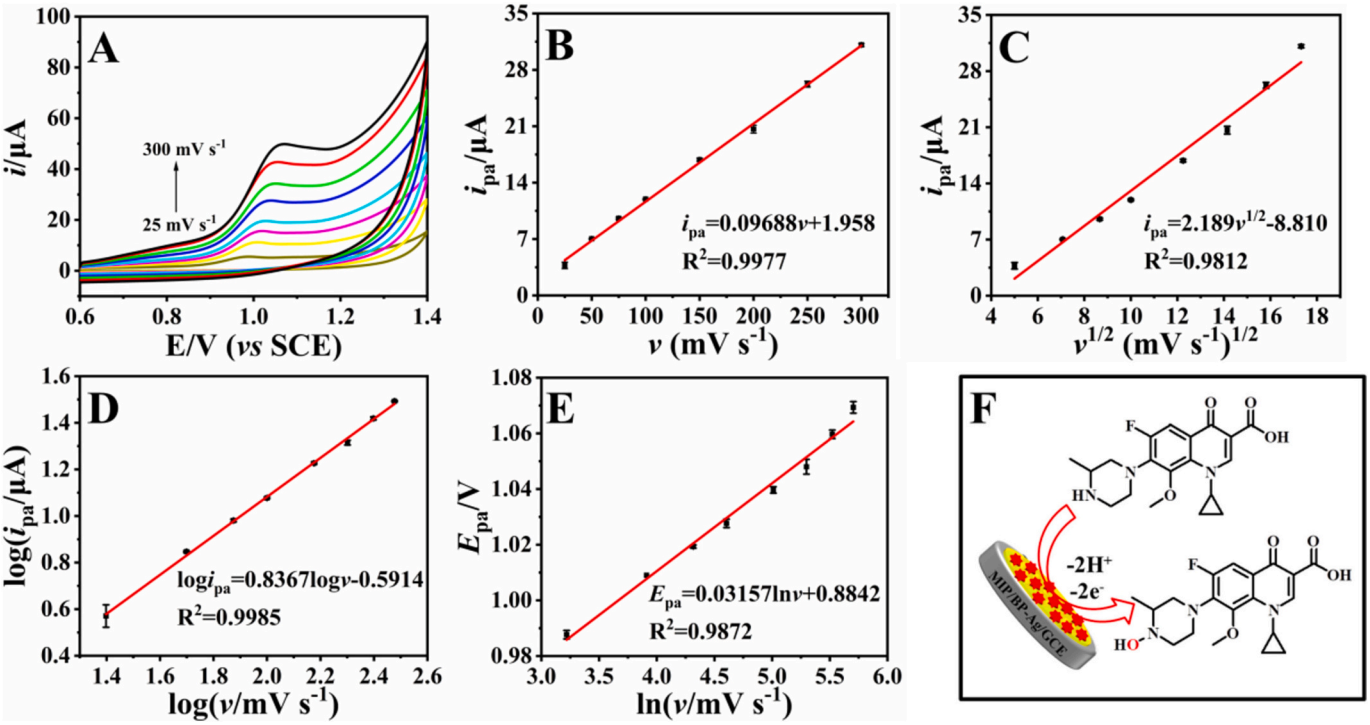

Fig. 3. (A) CV profiles of 10 μM GAT recorded at v = 25–300 mV s^{-1} for MIP/BPNS-AgNP/GCE; Linear plots of (B) i_{pa} vs. v, (C) i_{pa} vs. $v^{1/2}$, (D) log i_{pa} vs. log v, and (E) E_{pa} vs. ln v; (F) GAT electrooxidation mechanism at MIP/BPNS-AgNP/GCE.

different electrodes at open-circuit potential. When the GCE surface was coated with the BPNS, the R_{ct} decreased from 556.4 to 409.9 Ω because of the high conductivity of the BPNS (Fig. 2D). The plot of BPNS-AgNP/GCE showed a much smaller semicircle (R_{ct} = 105.8 Ω), indicating that BPNS-AgNP greatly promoted electron transfer. After modification by BPNS-AgNP/GCE and bare GCE with GAT-imprinted PPy, the R_{ct} increased to 1830 and 3594 Ω, respectively. This result reflected the low conductivity of the MIP membrane, which hinders electron transfer. After removing the templates, the R_{ct} of MIP/BPNS-AgNP/GCE reduced to 1092 Ω, consistent with the successful formation of imprinted cavities on the PPy membrane. In contrast, the R_{ct} values of NIP/GCE (4309 Ω) and NIP/BPNS-AgNP/GCE (2053 Ω) were considerably higher than those of their corresponding MIP counterparts, indicating a much stronger barrier to electron transfer.

3.4. Electrochemical response to GAT

The LSV plots for10 μM GAT at the different electrodes and their corresponding i_{pa} values are shown in Fig. 2E and F, respectively. The GAT peak current (i_{pa} = 0.2613 μA, curve a) was very low for the bare GCE owing to slow electrochemical kinetics. The response improved to i_{pa} = 1.057 μA (curve b) for BPNS-AgNP/GCE, which reflects the enhanced electrocatalytic activity of BPNS. When an imprinted PPy membrane was loaded onto the GCE, BPNS/GCE, and BPNS-AgNP/GCE platforms, the GAT peak currents increased to 3.016, 6.327, and 17.19 μA, respectively. These improvements reflect the strong adsorption capability and selective recognition ability of the imprinted PPy membrane. The GAT peak current for MIP/BPNS-AgNP/GCE (i_{pa} = 17.19 μA, curve e) was more than four times higher than that for MIP/GCE (i_{pa} = 3.016 μA, curve c), because BPNS-AgNP possessed a large surface area for the incorporation of more imprinted cavities, enhanced electrochemical activity, and expedited electron transport rate. On the contrary, the GAT peak currents for NIP/GCE and NIP/BPNS-AgNP/GCE were almost undetectable because of the low NIP-membrane conductivity.

3.5. Electrooxidation mechanism of GAT

The electrooxidation mechanism of GAT on MIP/BPNS-AgNP/GCE was investigated by CV after 10 min incubation in 10 μM GAT and transfer to 0.1 M PBS. Fig. 3A shows the CV profiles of 10 μM GAT at the scanning rates (v) of 0.025–0.3 V s^{-1}. On the forward scan, the anodic peaks shifted towards more positive potentials and i_{pa} increased with increasing v. No cathodic peaks were detected on the reverse scans, indicating an irreversible process for electrochemical GAT oxidation. Fig. 3B shows that the peak current of GAT oxidation correlated linearly with v (i_{pa}(μA) = 0.9688 v + 1.958, R^2 = 0.9977), which agrees well with an electrode reaction limited by adsorption. However, the i_{pa} of GAT is also linear to $v^{1/2}$ (Fig. 3C, i_{pa}(μA) = 2.189 $v^{1/2}$–8.810 (R^2 = 0.9812)), which coincides well with an electrode reaction limited by diffusion. Fig. 3D reveals that a linear log i_{pa} vs. log v plot yields a regression equation of log i_{pa} = 0.8367 log v − 0.5914 (R^2 = 0.9985). Therefore, the electrochemical GAT oxidation is considered to be a combination of the adsorption- and diffusion-controlled processes. Fig. 3E shows that the E_{pa} of GAT was proportional to ln$v$ and yielded a linear regression equation of E_{pa}(V) = 0.03157 ln v (mV s^{-1}) + 0.8841 (R^2 = 0.9872). Utilizing the Laviron equation(Laviron, 1979), the number of electrons transferred (n) in GAT electrooxidation was approximately 2, which is the same as the number of protons released in the electrode reaction. Therefore, we conclude that two proton losses and two electron transfers occur during GAT electrooxidation, which is in good agreement with previous studies (Wan et al., 2023; Zhu et al., 2020). A proposed electrooxidation mechanism of GAT on MIP/BPNS-AgNP/GCE is described in Fig. 3F. Generally, GAT oxidation often occurs on the second N4 amine on the piperazine ring. Therefore, the hydroxyl group might add on the N4 atom to form a hydroxylamine during GAT electrooxidation.

3.6. Electroanalytical performance

3.6.1. Calibration plots

The LSV responses to various concentrations of GAT recorded under

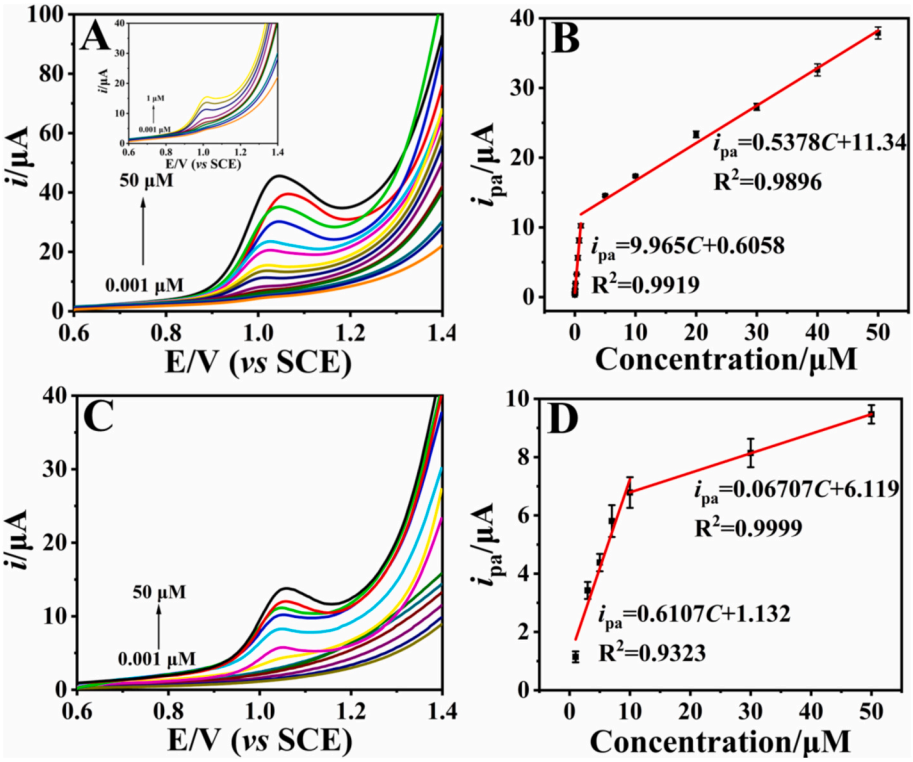

Fig. 4. LSV plots of (A) MIP/BPNS-AgNP/GCE and (C) NIP/BPNS-AgNP/GCE after incubation with 0.001–50 μM GAT solutions for 10 min. Plots of GAT i_{pa} in (B) panel A and i_{pa} in (D) panel C versus GAT concentration.

the optimal conditions for MIP/BPNS-AgNP/GCE are presented in Fig. 4A. Fig. 4B shows the two regions of linear response in the concentration ranges of 0.001–1 and 1–50 μM. The linear regression equations in the low- and high-concentration regions are $i_{pa}(\mu A) = 9.965C(\mu M) + 0.6058$ ($R^2 = 0.9919$) and $i_{pa}(\mu A) = 0.5378C(\mu M) + 11.34$ ($R^2 = 0.9896$), respectively. The LOD at 3σ/S, where σ and S denote the standard deviation of blank solution measurements and the slope of calibration plot at low-concentration region, is 0.2 nM for MIP/BPNS-AgNP/GCE. Fig. 4C shows the LSV curves for 0.001–30 μM GAT oxidation at NIP/BPNS-AgNP/GCE. NIP/BPNS-AgNP/GCE exhibited a detectable peak current only when the GAT concentration exceeded 1 μM and showed two regions of linear response (Fig. 4D). The linear regression equations for the low-concentration (1–10 μM) and high-concentration (10–50 μM) regions were $i_{pa}(\mu A) = 0.6107C(\mu M) + 1.132$ ($R^2 = 0.9323$) and $i_{pa}(\mu A) = 0.06707C(\mu M) + 6.119$ ($R^2 = 0.9999$), respectively. NIP/BPNS-AgNP/GCE demonstrated considerably narrower linear response ranges, lower sensitivity and a worse LOD (0.45 μM) than MIP/BPNS-AgNP/GCE, indicating the strong sensing ability of the MIP/BPNS-AgNP. Table S1 shows that the electroanalytical performance of MIP/BPNS-AgNP/GCE is comparable with those of other electrochemical detection methods of GAT.

3.6.2. *Interfering substances*

A principal advantage of MIP electrodes is their high specificity. In order to evaluate the anti-interference property of MIP/BPNS-AgNP/GCE, GAT structural analogs and interfering substances present in serum (Fig. S3) were chosen as potential interfering substances. The LSV curves after separate incubation in 5 μM GAT and potential interfering substances are shown in Fig. S4A. No oxidation peaks were apparent after incubation in 5 μM PEN-G, TET, AMO, DOP, UA, LYS, AA, and GLU (Fig. S4B), suggesting that minimal binding of these substances occurs in the MIP membrane. Peak currents were observed after incubation in ENR, NOR, MAR, LOME, LEV, and OFL; however, the values were considerably lower than those after GAT incubation. Thus, these interfering substances were not bound as extensively as GAT in the imprinted cavities. The GAT peak currents were measured in the presence of potential interfering substances to further evaluate its anti-interference ability (Table S2). The relative error in GAT detection by MIP/BPNS-AgNP/GCE in the presence of five-fold excesses of interfering substances ranged from 0.664 % to 3.72 %. The relative error increased to 1.92 %–4.84 % in coexistence with 10-fold excesses of the interfering substances. Thus, MIP/BPNS-AgNP/GCE exhibited a strong preference for GAT and can be used to selectively detect GAT in complex mixtures.

3.6.3. *Repeatability, reproducibility, and stability*

The repeatability, reproducibility, and stability of a MIP sensing platform is critical for practical applications. It is therefore worth investigating these properties. LSV plots for 10 continuous determinations of 5 μM GAT were almost identical (Fig. S4C), and the relative standard deviation (RSD) was 2.47 %. The reproducibility of the method was found to be good. LSV plots for 5 μM GAT recorded by five independent MIP/BPNS-AgNP/GCE systems almost coincide (Fig. S4D). The RSD of the measurements using five independent MIP/BPNS-AgNP/GCE systems was 3.64 % (Fig. S4E). LSV plots for 5 μM GAT within 26 days almost overlap (Fig. S4F). The peak current of 5 μM GAT retained 93.6 % of its initial value after 26 days (Fig. S4G), which confirms the stability of the MIP/BPNS-AgNP/GCE system. Moreover, the stability of the exfoliated BPNS in mixed ferri−/ferrocyanide solution was investigated. Fig. S4H shows that the peak currents gradually decreased at BPNS/GCE with increase in the number of cycles. After 2000 continual scans, the i_{pa} and i_{pc} of $[Fe(CN)_6]^{3-/4-}$ reduced by 58.55 % and 62.42 %, respectively, indicating the low stability of the isolated BPNS. However, these peak currents decreased by only 7.12 % and 9.38 % following 2000 consecutive scans at BPNS-AgNP/GCE (Fig. S4I). Thus, the AgNP functionalization contribute to detector stability. The strong ability of BP or P_xO_y species to form chelates with AgNPs significantly prevent the degradation of BP in aqueous solution (Li et al., 2022a; Li et al., 2024a), thereby achieving a robust response to GAT.

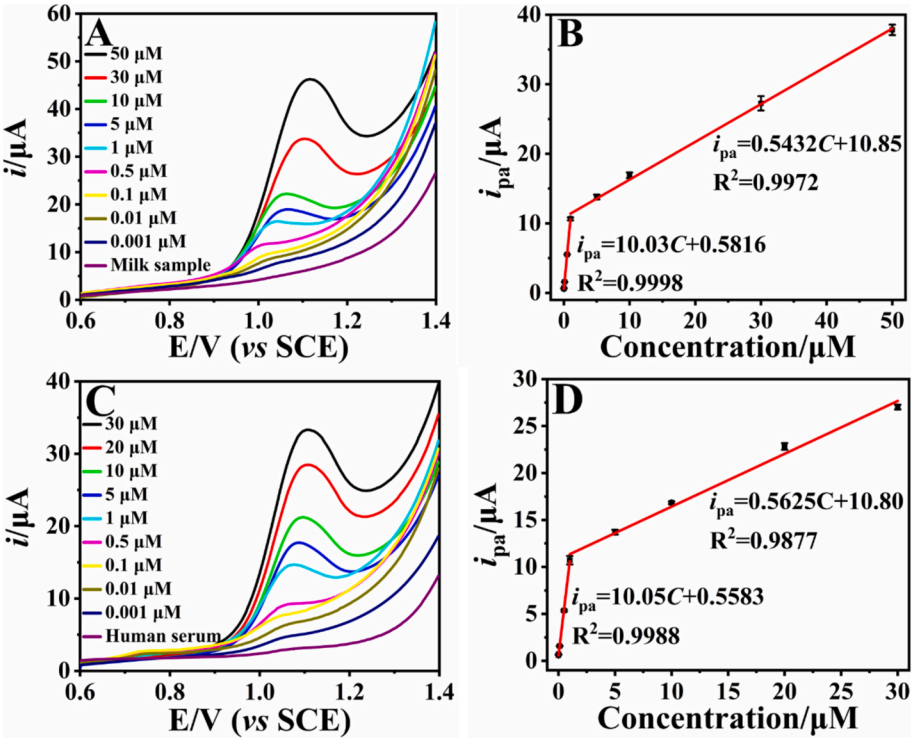

Fig. 5. LSV plots for MIP/BPNS-AgNP/GCE after incubation in milk samples containing 0.001–50 μM GAT (A) and human serum samples containing 0.001–30 μM GAT (C) for 10 min. Plots of i_{pa} in panel A (B) and i_{pa} in panel C (D) versus concentration.

3.6.4. Determination of GAT in actual samples

Actual samples were analyzed for GAT via LSV to validate the practicability of MIP/BPNS-AgNP/GCE systems for GAT detection. Table S3 shows that the concentration of GAT detected in the pharmaceutical preparations was consistent with the labeled value, with satisfactory relative error and RSD results. The recoveries of the pharmaceuticals by standard addition were 99.76 % and 98.86 %. The findings confirm that MIP/BPNS-AgNP/GCE can accurately quantitate GAT in drugs.

Fig. 5A presents the LSV curves for different concentrations of GAT in milk. No GAT residues were detected in the milk samples. Table S4 shows that the standard recoveries in milk were 99.13 %–102.6 %, with RSDs of <5 %. The GAT peak current was linear to concentration over two ranges: 0.001–1 and 1–50 μM (Fig. 5B), identical to the behavior observed in the PBS solution. The linear equations in the low- and high-concentration ranges are $i_{pa} = 10.03C + 0.5816$ ($R^2 = 0.9998$) and $i_{pa} = 0.5432C + 10.85$ ($R^2 = 0.9972$), respectively. The sensitivity toward GAT in milk samples is not significantly different from that in PBS, indicating that GAT detection is not affected by the milk matrix.

Recoveries in the human serum samples were 95.33 %–103.0 %, with RSDs below 5 % (Table S5). Fig. 5C shows the absence of a GAT peak in the serum sample, indicating that the GAT concentration in the serum is zero or below the LOD of the method. Fig. 5D shows that the GAT peak current was linear to the concentration (0.001–1 and 1–30 μM). The linear range in the serum matrix was slightly narrower than that in PBS; however, the sensitivity was nearly equal to that in PBS. Thus, GAT detection by the MIP/BPNS-AgNP/GCE systems was not affected by the serum matrix. It should be noted that GAT concentration in milk and serum lower than 0.01 M cannot be detected by HPLC. At higher concentration region, the detection results for both milk and serum are consistent with those detected by HPLC.

4. Conclusion

In conclusion, an ultrasensitive MIP voltammetric platform based on BPNS-AgNP was developed for the selective determination of GAT in pharmaceutical preparations, milk, and human serum samples. BPNS-AgNP improved the ambient stability, electrical conductivity, and electrochemical activity of the BPNS and possessed a large surface area for accommodating abundant templates to produce specific imprinted sites. Under the optimal conditions, the MIP/BPNS-AgNP/GCE assembly displayed extraordinary electroanalytical performance for GAT, with two wide linear response ranges of 0.001–1 and 1–50 μM and high sensitivities of 9.965 and 0.5378 μA μM^{-1}. The LOD was down to 0.2 nM. The MIP/BPNS-AgNP/GCE realized the selective determination of GAT in the presence of structurally and functionally similar interfering substances. The sensor was confirmed to be repeatable, reproducible, and stable and could detect GAT in pharmaceutical formulations, milk, and human serum. This study described a protocol for sensitive and selective detection of GAT in complex matrices such as food and physiological fluids and a new strategy for the design of MIP voltammetric sensors for fluoroquinolone.

CRediT authorship contribution statement

Jingtao Wu: Writing – original draft, Investigation, Data curation, Conceptualization. **Yonghui Xia:** Methodology, Investigation, Funding acquisition, Data curation. **Tianyu Wang:** Funding acquisition, Formal analysis, Data curation. **Yafeng Zhang:** Visualization, Validation. **Guangli Li:** Writing – review & editing, Methodology, Funding acquisition, Conceptualization.

Declaration of competing interest

The authors declare that they have no known competing financial interests or personal relationships that could have appeared to influence the work reported in this paper.

Data availability

Data will be made available on request.

Acknowledgment

This work was financially supported by the National Natural Science Foundation of China (62176089), Hunan Provincial Natural Science Foundation (2023JJ20024; 2022JJ80123; 2021JJ30226), Scientific Research Foundation of Hunan Province Education Department (21B0532), and Postgraduate Scientific Research Innovation Project of Hunan Province (CX20240915). The authors would like to thank Editage (http://www.editage.cn) for English language editing. The authors would also like to thank Shiyanjia Lab (www.shiyanjia.com) for the XPS spectra, Raman spectra and zeta potential analysis.

Appendix A. Supplementary data

Supplementary data to this article can be found online at https://doi.org/10.1016/j.fochx.2024.102094.

References

Abate, Y., Akinwande, D., Gamage, S., Wang, H., Snure, M., Poudel, N., & Cronin, S. B. (2018). Recent progress on stability and passivation of black phosphorus. *Advanced Materials, 30*(29), Article 1704749.

Anju, S., Ashtami, J., & Mohanan, P. V. (2019). Black phosphorus, a prospective graphene substitute for biomedical applications. *Materials Science and Engineering: C, 97*, 978–993.

Caianelo, M., Espíndola, J. C., Diniz, V., Spina, M., Rodrigues-Silva, C., & Roberto Guimarães, J. (2022). Gatifloxacin photocatalytic degradation in different water matrices: Antimicrobial activity and acute toxicity reduction. *Journal of Photochemistry and Photobiology A: Chemistry, 430*, Article 113973.

Caporali, M., Serrano-Ruiz, M., Telesio, F., Heun, S., Verdini, A., Cossaro, A., … Peruzzini, M. (2020). Enhanced ambient stability of exfoliated black phosphorus by passivation with nickel nanoparticles. *Nanotechnology, 31*(27), Article 275708.

Chen, J., Yang, Y., Zhao, S., Bi, F., Song, L., Liu, N., … Zhang, X. (2022). Stable black phosphorus encapsulation in porous mesh-like UiO-66 promoted charge transfer for photocatalytic oxidation of toluene and o-dichlorobenzene: Performance, degradation pathway, and mechanism. *ACS Catalysis, 12*(13), 8069–8081.

Cho, S.-Y., Koh, H.-J., Yoo, H.-W., & Jung, H.-T. (2017). Tunable chemical sensing performance of black phosphorus by controlled functionalization with Noble metals. *Chemistry of Materials, 29*(17), 7197–7205.

Cui, B., Liu, P., Liu, X., Liu, S., & Zhang, Z. (2020). Molecularly imprinted polymers for electrochemical detection and analysis: Progress and perspectives. *Journal of Materials Research and Technology, 9*(6), 12568–12584.

Ge, X., Xia, Z., & Guo, S. (2019). Recent advances on black phosphorus for biomedicine and biosensing. *Advanced Functional Materials, 29*(29), Article 1900318.

Hasseb, A. A., Abdel Ghani, N.d. T., Shehab, O. R., & El Nashar, R. M. (2022). Application of molecularly imprinted polymers for electrochemical detection of some important biomedical markers and pathogens. *Current Opinion in Electrochemistry, 31*, Article 100848.

Jiang, L., Mo, G., Yu, C., Ya, D., He, X., Mo, W., & Deng, B. (2019). Based on reduced graphene oxide-copper sulfide-carbon nitride nanosheets composite electrochemiluminescence sensor for determination of gatifloxacin in mouse plasma. *Colloids and Surfaces B: Biointerfaces, 173*, 378–385.

Laviron, E. (1979). General expression of the linear potential sweep voltammogram in the case of diffusionless electrochemical systems. *Journal of Electroanalytical Chemistry and Interfacial Electrochemistry, 101*(1), 19–28.

Lei, W., Zhang, T., Liu, P., Rodriguez, J. A., Liu, G., & Liu, M. (2016). Bandgap- and local field-dependent photoactivity of Ag/black phosphorus nanohybrids. *ACS Catalysis, 6*(12), 8009–8020.

Li, G., Qi, X., Wu, J., Wan, X., Wang, T., Liu, Y., … Xia, Y. (2024a). Highly stable electrochemical sensing platform for the selective determination of pefloxacin in food samples based on a molecularly imprinted-polymer-coated gold nanoparticle/black phosphorus nanocomposite. *Food Chemistry, 436*, Article 137753.

Li, G., Qi, X., Wu, J., Xu, L., Wan, X., Liu, Y., … Li, Q. (2022a). Ultrasensitive, label-free voltammetric determination of norfloxacin based on molecularly imprinted polymers and Au nanoparticle-functionalized black phosphorus nanosheet nanocomposite. *Journal of Hazardous Materials, 436*, Article 129107.

Li, G., Wan, X., Zheng, Q., Yang, M., Xia, Y., Qi, X., … Wu, Z. (2024b). Deep eutectic solvent-mediated synthesis of ZnCo2O4/MWCNT-COOH: Investigation of electrocatalytic activity for gatifloxacin detection. *Colloids and Surfaces A: Physicochemical and Engineering Aspects, 699*, Article 134713.

Li, G., Wu, J., Qi, X., Wan, X., Liu, Y., Chen, Y., & Xu, L. (2022b). Molecularly imprinted polypyrrole film-coated poly(3,4-ethylenedioxythiophene):Polystyrene sulfonate-functionalized black phosphorene for the selective and robust detection of norfloxacin. *Materials Today Chemistry, 26*, Article 101043.

Li, Q., Wu, J.-T., Liu, Y., Qi, X.-M., Jin, H.-G., Yang, C., … He, Q.-G. (2021). Recent advances in black phosphorus-based electrochemical sensors: A review. *Analytica Chimica Acta, 1170*, Article 338480.

Liu, B., Su, Y., Wu, S., & Shen, J. (2021). Two dimensional BP@AuNP nanocomposites for photothermal/photodynamic therapy mediated wound disinfection and infected wound healing under a single light source. *New Journal of Chemistry, 45*(38), 18124–18130.

Liu, M., Feng, S., Hou, Y., Zhao, S., Tang, L., Liu, J., … Liu, B. (2020). High yield growth and doping of black phosphorus with tunable electronic properties. *Materials Today, 36*, 91–101.

Liu, S., Luo, J., Jiang, X., Li, X., & Yang, M. (2020). Gold nanoparticle–modified black phosphorus nanosheets with improved stability for detection of circulating tumor cells. *Microchimica Acta, 187*(7), 397.

Liu, W., Zhu, Y., Ban, X., Wang, S., & Zhu, H. (2021). Ag/black phosphorus composite based on multilayer black phosphorus: Its preparation and photocatalytic methyl orange degradation performance. *Materials Science in Semiconductor Processing, 121*, Article 105309.

Liu, X., Chen, K., Li, X., Xu, Q., Weng, J., & Xu, J. (2021). Electron matters: Recent advances in passivation and applications of black phosphorus. *Advanced Materials, 33*(50), Article 2005924.

Ma, Q., Cong, W., Liu, Y., Geng, Z., Lin, Y., & Wang, Z. (2021). Experimental and computational study on the enantioseparation of four chiral fluoroquinolones by capillary electrophoresis with sulfated-β-cyclodextrin as chiral selector. *Chirality, 33*(9), 549–557.

Qiu, S., Liang, J., Hou, Y., Zhou, X., Zhou, Y., Wang, J., … Hu, Y. (2022). Hindered phenolic antioxidant passivation of black phosphorus affords air stability and free radical quenching. *Journal of Colloid and Interface Science, 606*, 1395–1409.

Razavipanah, I., Alipour, E., Deiminiat, B., & Rounaghi, G. H. (2018). A novel electrochemical imprinted sensor for ultrasensitive detection of the new psychoactive substance "Mephedrone". *Biosensors and Bioelectronics, 119*, 163–169.

Ryder, C. R., Wood, J. D., Wells, S. A., Yang, Y., Jariwala, D., Marks, T. J., … Hersam, M. C. (2016). Covalent functionalization and passivation of exfoliated black phosphorus via aryl diazonium chemistry. *Nature Chemistry, 8*(6), 597–602.

Saad, M. N., Essam, H. M., Elzanfaly, E. S., & Amer, S. M. (2020). A two-step optimization approach: Validated RP-HPLC method for determination of Gatifloxacin and dexamethasone in ophthalmic formulation. *Journal of Chromatographic Science, 58*(6), 504–510.

Shoueir, K., Mohanty, A., & Janowska, I. (2022). Industrial molasses waste in the performant synthesis of few-layer graphene and its Au/Ag nanoparticles nanocomposites. Photocatalytic and supercapacitance applications. *Journal of Cleaner Production, 351*, Article 131540.

Sumalatha, V., & Ayodhya, D. (2023). Fabrication and characterization of CuO nano-needles from thermal decomposition of Cu(II) metal complex: Fluorometric detection of antibiotics, antioxidant, and antimicrobial activities. *Results in Chemistry, 5*, Article 100821.

Sversut, R. A., Alcântara, I. C., Rosa, A. M., Baroni, A. C. M., Rodrigues, P. O., Singh, A. K., … Kassab, N. M. (2017). Simultaneous determination of gatifloxacin and prednisolone acetate in ophthalmic formulation using first-order UV derivative spectroscopy. *Arabian Journal of Chemistry, 10*(5), 604–610.

Taherizadeh, M., Jahani, S., Moradalizadeh, M., & Foroughi, M. M. (2023). Synthesis of a dual-functional terbium doped copper oxide nanoflowers for high-efficiently electrochemical sensing of ofloxacin, pefloxacin and gatifloxacin. *Talanta, 255*, Article 124216.

Takeuchi, Y., Lee, H. J., Dao, A. T. N., Kasai, H., Teranishi, R., & Kaneko, K. (2021). Formation of multishell Au@Ag@Pt nanoparticles by coreduction method: A microscopic study. *Materials Today Chemistry, 21*, Article 100515.

Tian, Y., Wang, H., Li, H., Guo, Z., Tian, B., Cui, Y., … Wu, Y. (2020). Recent advances in black phosphorus/carbon hybrid composites: From improved stability to applications. *Journal of Materials Chemistry A, 8*(9), 4647–4676.

Uddin, T. M., Chakraborty, A. J., Khusro, A., Zidan, B. M. R. M., Mitra, S., Emran, T. B., … Koirala, N. (2021). Antibiotic resistance in microbes: History, mechanisms, therapeutic strategies and future prospects. *Journal of Infection and Public Health, 14*(12), 1750–1766.

Van Doorslaer, X., Dewulf, J., Van Langenhove, H., & Demeestere, K. (2014). Fluoroquinolone antibiotics: An emerging class of environmental micropollutants. *Science of the Total Environment, 500-501*, 250–269.

Wan, L., Wu, Y., Zhang, Y., & Zhang, W. (2022). Toxicity, biodegradation of moxifloxacin and gatifloxacin on *Chlamydomonas reinhardtii* and their metabolic fate. *Ecotoxicology and Environmental Safety, 240*, Article 113711.

Wan, X., Du, H., Tuo, D., Qi, X., Wang, T., Wu, J., & Li, G. (2023). UiO-66/carboxylated multiwalled carbon nanotube composites for highly efficient and stable voltammetric sensors for Gatifloxacin. *ACS Applied Nano Materials, 6*(20), 19403–19413.

Wang, J., Zhang, S., Ma, S., Hao, X., Li, X., & Xu, B. (2024). Silver nanoparticle-modified black phosphorus for photocatalytic properties. *ACS Applied Nano Materials, 7*(6), 6178–6184.

Wang, T., Xia, Y., Wan, X., Zhang, Y., Chen, N., Jin, Y., & Li, G. (2024). A facile and efficient voltammetric sensor for marbofloxacin detection based on zirconium-based metal-organic framework UiO-66/nitrogen-doped graphene nanocomposite. *Microchemical Journal, 201*, Article 110673.

Wang, Y., Zhou, Y., Li, J., Zhang, R., Zhao, H., & Wang, Y. (2022). Ag decoration-enabled sensitization enhancement of black phosphorus nanosheets for trace NO2 detection at room temperature. *Journal of Hazardous Materials, 435*, Article 129086.

Wu, Y., Li, G., Tian, Y., Feng, J., Xiao, J., Liu, J., … He, Q. (2021). Electropolymerization of molecularly imprinted polypyrrole film on multiwalled carbon nanotube surface

for highly selective and stable determination of carcinogenic amaranth. *Journal of Electroanalytical Chemistry, 895*, Article 115494.
Xu, S., Lin, G., Zhao, W., Wu, Q., Luo, J., Wei, W., … Zhu, Y. (2018). Necklace-like molecularly imprinted nanohybrids based on polymeric nanoparticles decorated multiwalled carbon nanotubes for highly sensitive and selective melamine detection. *ACS Applied Materials & Interfaces, 10*(29), 24850–24859.
Yu, K., Yue, M.-E., Xu, J., & Jiang, T.-F. (2020). Determination of fluoroquinolones in milk, honey and water samples by salting out-assisted dispersive liquid-liquid microextraction based on deep eutectic solvent combined with MECC. *Food Chemistry, 332*, Article 127371.
Zhang, Z., Li, Y., Xu, J., & Wen, Y. (2018). Electropolymerized molecularly imprinted polypyrrole decorated with black phosphorene quantum dots onto poly(3,4-ethylenedioxythiophene) nanorods and its voltammetric sensing of vitamin C. *Journal of Electroanalytical Chemistry, 814*, 153–160.
Zhu, M., Li, R., Lai, M., Ye, H., Long, N., Ye, J., & Wang, J. (2020). Copper nanoparticles incorporating a cationic surfactant-graphene modified carbon paste electrode for the simultaneous determination of gatifloxacin and pefloxacin. *Journal of Electroanalytical Chemistry, 857*, Article 113730.